Asociación Argentina
de Mecánica Computacional

Mecánica Computacional Vol XXVII, págs. 3225-3245 (artículo completo)
Alberto Cardona, Mario Storti, Carlos Zuppa. (Eds.)
San Luis, Argentina, 10-13 Noviembre 2008

DELAYED DETACHED EDDY SIMULATION OF FLOW OVER AN AIRFOIL WITH SYNTHETIC JET CONTROL

Omar D. Lopez and Robert D. Moser

Department of Mechanical Engineering, University of Texas at Austin, 1 University station C2200, Austin, TX 78712-0292. odlopez@mail.utexas.edu, **http://www.me.utexas.edu**

Keywords: Delayed detached eddy simulation, synthetic jet, flow control.

Abstract. Delayed Detached-Eddy Simulation (DDES) is a hybrid Reynolds-Averaged Navier Stokes/Large Eddy Simulation (RANS/LES) model similar to Detached-Eddy Simulation (DES) but with some modifications to reduce the influences of ambiguous grid densities in the numerical results. This model was implemented in CDP, a parallel unstructured grid incompressible flow solver, developed at the Center for Integrated Turbulence Simulations (CITS) at Stanford University. CDP has the advantage of being nearly energy conserving. Several simulations and validations of static cases in a modified NACA 4415 were performed. Implementation/validation of two different synthetic jet models (detail and Reynolds stress based) are presented. The detail model resolved the synthetic jet dynamics in time while the Reynolds stress model tries to capture the major effects that the synthetic jet induces in the flow. The Reynolds-stress synthetic jet model is based on experimental Particle Image Velocimeter (PIV) data and also on numerical data from the detail model. Numerical results show the effects of the actuators on the vortical structure of the flow, as well as on the aerodynamic properties.

1 INTRODUCTION

Flow control is simply a process to change the behavior of a flow field to meet some objective. A variety of methods can be used to achieve different effects such as : delay or advance transition, prevent or provoke separation; or suppress or enhance turbulence. Example of objectives could be drag reduction, lift enhancement, mixing improvement, noise suppression, among others. This paper presents a computational study of active flow control of a NACA4415 airfoil using synthetic jet actuators for lift and moment control.

Originally introduced by Ingard (1953) for acoustic problems, a synthetic jet actuator is a device that alternatively injects and removes fluid through a small orifice at a given frequency, so that the net mass addition to the flow is zero but its net momentum flux is not zero. It consists of an oscillating diaphragm driven by piezoelectric element and located in an small cavity. Synthetic jets actuators have been used in a variety of flow control applications such as separation control, control of jets, small scale control of turbulence and flight control dynamics of aircrafts since 1998 (Smith and Glezer, 1998; Parekh et al., 2003; Brzozowski and A.Glezer, 2006). DeSalvo and Glezer (2004) at Georgia Tech have shown that synthetic jet actuators are an effective way to enhance the lift and modify the moments of wings and airfoils. Effective control has been achieved with actuation frequencies an order of magnitude larger than the natural shedding frequency of the body (Amitay et al., 2001).

The simulation and modeling of synthetic jet actuators is a very active research field in the CFD community (Rumsey, 2008; Holman et al., 2005). These researches have shown that the success in the simulation of a synthetic jet depends on different factors such as: turbulent model, synthetic jet model and boundary conditions. It is also clear that one of the most important challenges that the simulation of synthetic jet has is the wide range of scales (spatial and temporal) that need to be resolved in this kind of problems. Despite of these challenges, numerical simulations tools have been used extensively for flow control problems with synthetic jets (Huang et al., 2004; Vadillo and Agarwal, 2006; Gross and Fasel, 2008). One important aspect in the simulation of turbulent flows is the numerical conservation of kinetic energy. Morishini et al. (1998) showed that the energy balance in turbulence and in LES models is rather delicate, so that numerics that interfere with the energy balance will yield incorrect results Reliable turbulence simulations for incompressible flows requires the use of numerical methods which retain the energy conservation characteristics of the convective and pressure terms of the Navier-Stokes equations. The development of LES and hybrid RANS-LES models allow simulation of the complex unsteady flow around an airfoil and can capture vortical structures over a wide range of turbulent scales. The Delayed Detached Eddy Simulation (DDES) model (Spalart et al., 2006) was selected as the hybrid RANS/LES model to be implemented on the CFD code.

This research is part of the AVOCET (Adaptive VOrticity Control Enabled flighT) project[1]. AVOCET is sponsored by the Air Force Office of Scientific Research (AFOSR) under the Multidisciplinary University Research Initiative (MURI). The main objective of the AVOCET project is to design and build closed-loop flow control with synthetic jet actuators for small scale Unmanned Aerial Vehicles (UAVs). Experimental and theoretical approaches are necessary to achieve this objective. Wind tunnel and flight experiments will provide the dynamic evolution of the forces and moments during dynamic tests with and without controlled actuation. This experimental part is being pursued at Georgia Tech. The theoretical part will support the design of the controller, sensor placement and provide details of the flow dynamics. Two different theoretical models will be developed: a low-order model based on vortex dynamics and a high-order

[1] http://www.avocet.gatech.edu/

CFD model, this paper is focused on the latter.

This paper is organized as follows: Section 2 describes the CFD code and the turbulent model used in this research. Section 3 explains the process of grid generation and the boundary conditions used in the computational model. In section 4, two different synthetic jet models are covered (detail and Reynolds stress models). Finally, section 5 shows the validation and discussion of the numerical results.

2 CFD CODE AND TURBULENT MODEL

2.1 CFD code (CDP)

As was mentioned in the introduction, the numerical conservation of kinetic energy plays an important role in the simulation of turbulent flows. This is one of the reasons, the unstructured grid incompressible flow solver CDP [2] was selected as the basic CFD tool in this research. CDP was developed at the Center for Integrated Turbulence Simulations (CITS) at Stanford University. CDP has been widely used in a variety of fluid flow problems and is one of the state of the art unstructured LES codes (Moin and Apte, 2004). Using CDP has several advantages such as:

- It is a nearly energy conserving solver
- It can be run as an standard LES code
- It is a parallel code that can be compile and execute in clusters and supercomputers showing good scalability up to thousands of CPUs
- It can handle hybrid meshes that can be partitioned with the standard ParMETIS library (Karypis and Kumar, 1997).

CDP uses a finite volume formulation of the Navier-Stokes equation. In this formulation, field variables such as velocity, pressure and scalars are cell centered associated while the normal velocity on the faces is face centered associated. CDP is based on the fractional-step method. In the first step, the cell centered velocity is predicted using the gradient of pressure from the previous time step. Then, the normal velocity is computed based on a simple interpolation of the predicted cell centered velocity. A Poisson equation for the pressure is solved using an Algebraic MultriGrid (AMG) Solver (this solver uses the Hypre library)[3]. Finally, the velocity is corrected based on the pressure field of the previous step. More details of the numerical method used on CDP can be found in Mahesh et al. (2004) and Iaccarino and Ham (2005)

2.2 Delayed Detached Eddy Simulation model (DDES)

In its standard implementation, DDES is based on the Spalart-Allmaras (SA) one-equation turbulence model. DDES is a modification of the Detached Eddy Simulation (DES) model (Spalart et al., 1998) to improve its performance in thick boundary layers and shallow separation regions. According to Spalart et al. (2006), for "ambiguous" grids DES shows premature transition between RANS and LES mode leading to artificial separation also known as Grid Induced Separation (GIS).

[2] http://www.stanford.edu/group/cits/research/combustor/cdp.html
[3] https://computation.llnl.gov/casc/linear_solvers/sls_hypre.html

Equation 1 shows the SA equation which is a convective-diffusive equation with some source terms to control the generation and destruction of the model variable $\tilde{\nu}$.

$$\frac{\partial \tilde{\nu}}{\partial t} + u_i \frac{\partial \tilde{\nu}}{\partial x_i} = c_{b1}\tilde{S}\tilde{\nu} + \frac{1}{\sigma}\left[\frac{\partial}{\partial x_i}\left((\nu+\tilde{\nu})\frac{\partial \tilde{\nu}}{\partial x_i}\right) + c_{b2}\left(\frac{\partial \tilde{\nu}}{\partial x_i}\right)^2\right] - c_{w1} f_w \left(\frac{\tilde{\nu}}{d}\right)^2 \tag{1}$$

The first term on the right hand side of the SA equation is a production term, the second one is diffusive term and the last one is a destruction term. $\tilde{\nu}$ and the eddy viscosity (ν_t) are related by $\nu_t = f_{v1}\tilde{\nu}$ where f_{v1} is given by equation 2.

$$f_{v1} = \frac{\chi^3}{\chi^3 + c_{v1}^3} \tag{2}$$

In equation 2, χ is the ratio of the model variable and the molecular viscosity i.e. $\chi \equiv \frac{\tilde{\nu}}{\nu}$. Equation 3 shows some relations needed to describe the production term of the SA equation.

$$\begin{aligned} \tilde{S} &\equiv S + \frac{\tilde{\nu}}{\kappa^2 d^2} f_{v2} \\ f_{v2} &= 1 - \frac{\chi}{1+\chi f_{v1}} \end{aligned} \tag{3}$$

In equation 3, S is the magnitude of the vorticity or the strain rate and d represents the distance to the wall. Equation 4 shows some relations needed to describe the destruction term of the SA equation.

$$\begin{aligned} f_w &= g\left[\frac{1+c_{w3}^6}{g^6 + c_{w3}^6}\right]^{\frac{1}{6}} \\ g &= r + c_{w2}(r^6 - r) \\ r &\equiv \frac{\tilde{\nu}}{\tilde{S}\kappa^2 d^2} \end{aligned} \tag{4}$$

Finally to complete the SA model several constants that appear in equations 2 - 4 must be defined. These constants are: $\kappa = 0.21$, $\sigma = 2/3$, $c_{b1} = 0.1355$, $c_{b2} = 0.622$, $c_{v1} = 7.1$, $c_{v2} = 5$, $c_{w1} = c_{b1}/\kappa^2 + (1+c_{b2})/\sigma$, $c_{w2} = 0.3$ and $c_{w3} = 2$

The DDES model is obtained by modifying the length scale in the SA model to be proportional to the grid size far from the wall (like LES), while remaining proportional to wall-distance near the wall. This is achieved by redefining d as it is shown in equation 5.

$$\begin{aligned} \tilde{d} &= d - f_d \max(0, d - C_{DES}\Delta) \\ f_d &= 1 - \tanh\left(8 r_d\right)^3 \\ r_d &= \frac{\tilde{\nu} + \nu}{\sqrt{U_{i,j}U_{i,j}}\kappa^2 d^2} \end{aligned} \tag{5}$$

In equation 5, Δ represents a characteristic grid size that, according to Travin et al. (1999), is normally defined as the diameter of the grid cell divided by $\sqrt{3}$. C_{DES} is a constant that is equal to 0.65 for homogeneous turbulence (Shur et al., 1999).

Several requirements had to be addressed in the implementation of DDES in the CDP code:

- The discretization of the convective and diffusive terms of the SA equation (equation 1) was done as it is described by Zwart (1999).
- The destruction and generation terms of the SA equation are treated as sources.
- The SA equation is solved before the first step of the fractional step method.
- One important characteristic of the discretization of the SA equation is its positivity i.e. the numerical scheme must ensure that $\tilde{\nu}$ is positive everywhere and at every time step (Spalart and Allmaras, 1994; Lorin et al., 2006). A non-positive $\tilde{\nu}$ not only represents a non-physical situation but also represents stability problems in the numerical scheme. A forward Euler scheme was used to preserve the positivity of the SA equation, similar time marching scheme for the SA equation has been used in other studies (Terzi et al., 2006; Spalart and Allmaras, 1994).
- Another important change of the original SA equation to preserve the positivity of $\tilde{\nu}$ is a new definition of $\tilde{S}$ (Squires et al., 2002; Deck et al., 2002). This modification consists of replacing equation 3 by equation 6

$$\begin{aligned} \tilde{S} &\equiv f_{v3} S + \frac{\tilde{\nu}}{\kappa^2 d^2} f_{v2} \\ f_{v2} &= \left(1 + \frac{\chi}{c_{v2}}\right)^{-3} \\ f_{v3} &= \frac{(1 + \chi f_{v1})(1 - f_{v2})}{\chi} \end{aligned} \tag{6}$$

- The non symmetric sparse matrix that is obtained from the discretization of the SA equation is solved via a BiConjugate Gradient Stabilized (Bi-CGSTAB) solver.
- A limiting algorithm had to be implemented to help preserve the positivity of $\tilde{\nu}$. This limiting algorithm consists of modifying the coefficients of the interpolation used in the discretization of the convective term of the SA equation. First, the algorithm identifies those cells in which $\tilde{\nu} < 0$. Then, the interpolation scheme is modified so that a fully upwind formulation is used on those problematic cells. This approach locally increases the numerical diffusion and it ensures the diagonal dominance of the matrix that goes into the BiCGSTAB solver.

Results from early test of the model showed high values of the eddy viscosity in the wake and in the separation region. Basically, the model was behaving as RANS in these regions. This observation has been reported previously in the DDES model by Deck (2008) and it is related to a slow transition from RANS to LES mode due to a extended grey-area, leading to a delay in the development of instabilities. A modification suggested by Breuer et al. (2003) was implemented to address this problem. This modification is achieved by postulating an equilibrium between the production and destruction of $\tilde{\nu}$ in the LES region, leading to the requirement that $f_{v1} = 1$, $f_{v2} = 0$ and $f_w = 1$ which is enforced in the wake far from the body. This approach is also known as Zonal DES and it was introduced by Deck (2005). Figure 1 shows on the left the eddy viscosity field without the modification and on the right with the implemented modification. A reduction of the magnitude of the eddy viscosity is observed in the wake and also more vorticity breakdown.

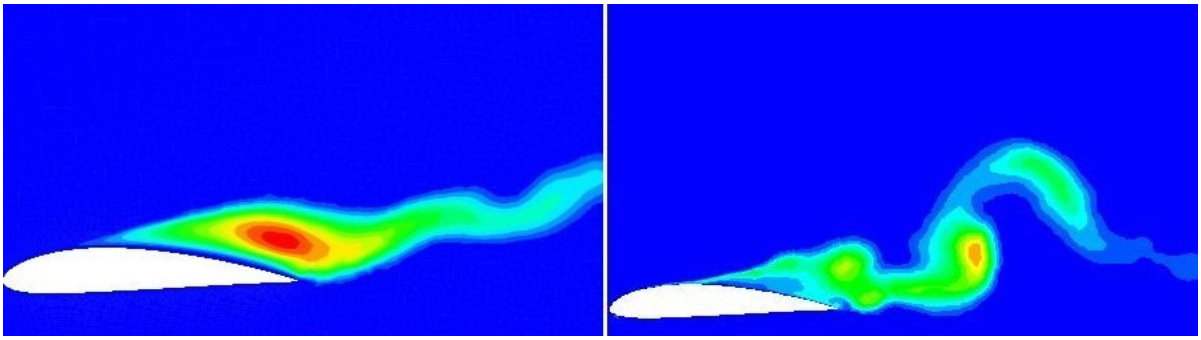

Figure 1: Eddy viscosity field at angle of attack of 30° and $Re = 5.7 \times 10^5$.

3 GRID GENERATION

The experimental set-up of Dr Glezer's lab at Georgia Tech was taken as baseline and it consists of a 18-in-chord modified NACA4415 with two tangential actuators mounted near the trailing edge, one in the pressure side (PS) and one in the suction side (SS). These actuators have a characteristic height of 0.017c and an effective jet outlet of 0.4 mm i.e. $8.5 \times 10^{-4}c$. These actuators are designed to affect the total circulation and to create a coanda effect near the trailing edge of the modified airfoil.

One important requirement for the DDES model is an appropriate mesh. The mesh plays an important role in the performance of the DDES model (Spalart, 2001). Basically, the characteristic mesh size determines the transition between the RANS and the LES zones and the size of the gray region. In order to satisfied these requirements a hybrid mesh was designed. This hybrid mesh allows a structured grid close to the airfoil surface (RANS region) and an unstructured grid on the rest of the domain(LES and Euler regions). The Reynolds number in the simulations is close to 1×10^6 so a grid spacing of O($1 \times 10^{-5}c$) was chosen in the direction normal to the wall so that the $y+$ of the first grid point is of order 1.5. Along the surface of the airfoil 150 grid points were used. These grid points were clustered towards the leading and the trailing edges giving a grid spacing of O($1 \times 10^{-2}c$) to O($1 \times 10^{-3}c$). The domain is one chord length in the spanwise direction. Since Δ_o (characteristic mesh size in the LES region) was chosen equal to 0.02c then fifty grid points were used in the span direction in order to produce an isotropic mesh in the LES region. Gridgen [4] is a commercial software that was used in the grid generation. Figure 2 shows the mesh created for this project, it contains around 1 million nodes. The different regions (RANS, LES, departure and Euler) that form the domain can be observed. Figure 3 shows the detail of the mesh in the RANS region; it also shows the transition between the structured and the unstructured grid zones. Figure 4 shows some details of the modified NACA4415 airfoil used in the experiments and it also shows the details of the modified mesh close to the airfoil surface to match this new geometry.

4 SYNTHETIC JET MODEL

Several models can be applied in the simulation of synthetic jets: reduced-order models, detail models or a simple boundary condition. According to Touber and Moser (2006) a vortex based reduced-order model a of a synthetic jet could represent the behavior of the jet very well, and that such a model could be coupled in to an Eulerian CFD code. Another possible reduced-order model is a Lumped Element Model (LEM) (Gallas et al., 2003) but the performance of

[4] http://www.pointwise.com/gridgen/

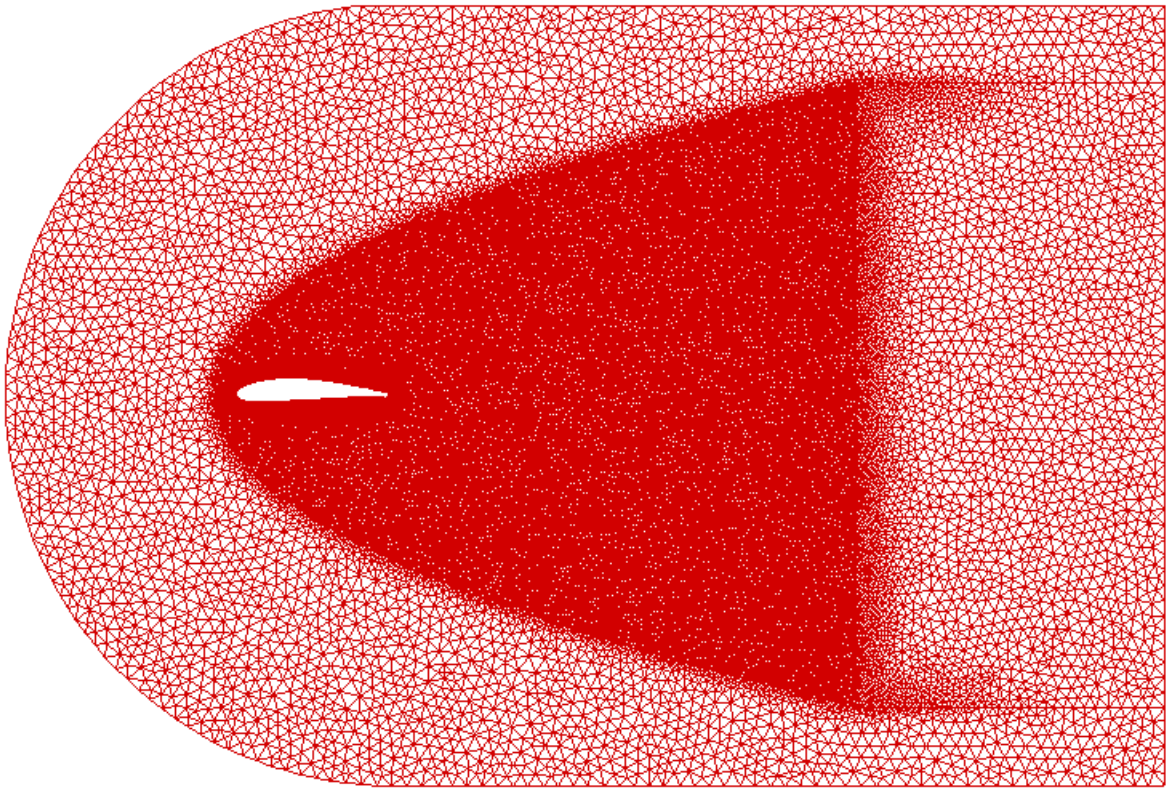

Figure 2: Mesh

these reduced-order models for a tangential jet would be highly dependent on modeling the interaction with the wall and with the cross flow, which would be more difficult. According to Mittal and Cattafesta (2008) it is also clear that using only a boundary condition at the synthetic jet outlet without resolving the cavity is not accurate enough. Two different models were used: a detail time-resolved synthetic jet model and a synthetic jet model based on an empirical Reynolds stress field induced by the actuator.

4.1 Detail model

This model consists on resolving the spatial and temporal detail of the synthetic jet. Figure 5 shows the cavity of the synthetic jet and the mesh used. This geometry was created as similar as possible to the actual cavity in the experimental set-up. In order to simulate the diaphragm oscillation a specified normal velocity is imposed on the lower boundary of the cavity (see Figure 5). Frequency and amplitude of this Dirichlet boundary condition will determine the momentum coefficient C_μ of the synthetic jet at the outlet. The momentum coefficient is defined as the ratio of jet momentum to free-stream momentum. The jet momentum can be defined using the peak velocity or the RMS velocity of the jet. In this case the RMS velocity was used i.e: $C_\mu \equiv \frac{U_{rms}^2 A_{jet}}{0.5 U_\infty^2 A}$.

4.2 Reynolds Stress Synthetic Jet (RSSJ) model

This model is based on the fact that the actuation frequencies are high compared to relevant flow time-scales. As was mentioned in the introduction, in order to achieve effective flow control the difference between the characteristic flow frequency and the actuation frequency must be about one order of magnitude. From experimental PIV data two major effects are

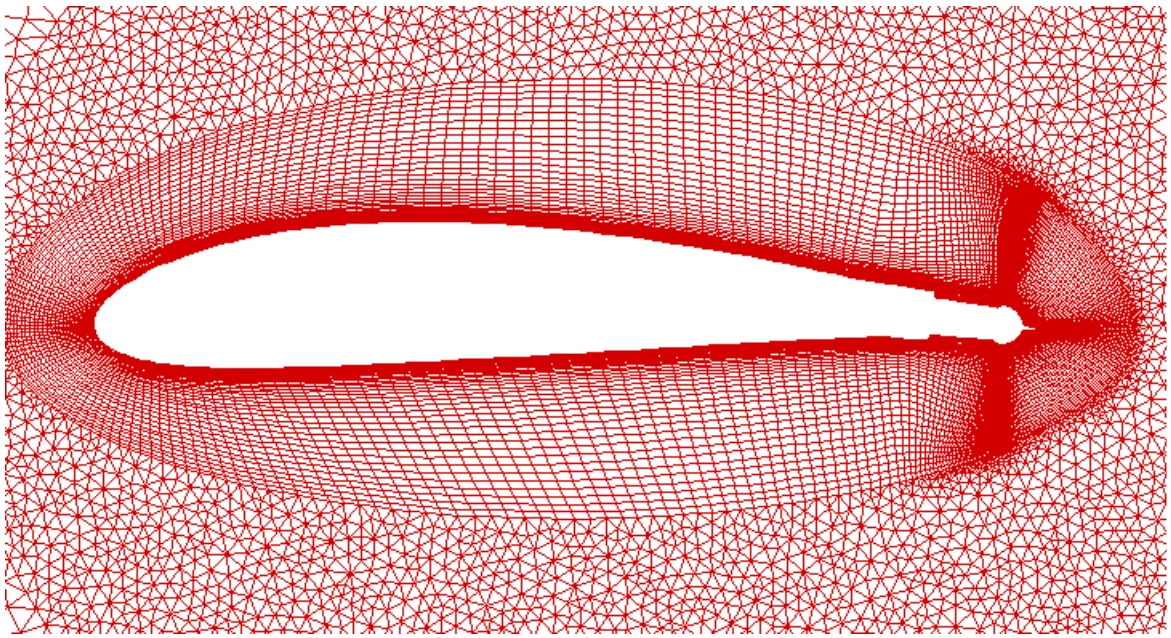

Figure 3: Detail of the mesh close to the airfoil

observed when the synthetic jet is active. First, a momentum flux in the synthetic jet outlet and second a modified Reynolds stress field. Experimental observations also suggest that the former effect is weaker, so the synthetic jet model implemented consists of a parameterized Reynolds stress field arising from the jet. Figure 6 shows a comparison between the experimental and the computational simulation of the averaged difference of the u'u' Reynolds stress component. In Figure 6, negative indicates that when the actuator is on the u'u' component decreases while positive indicates that this variable increases. It is clear that the effects close to the synthetic jet outlet are negligible in comparison with the effect on the far field. The divergence of the idealized Reynolds stress field was introduced as a momentum source in the Navier-Stokes solver to determine if this synthetic jet characterization was able to produce observed actuator effects.

5 NUMERICAL RESULTS

5.1 Validation of unactuated cases

Several static cases of the modified NACA4415 without the synthetic jets activated were performed. For these simulations the Reynolds number was fixed at 9×10^5 and the angle of attack (AoA) was changed from $0°$ up to $15°$. Figure 7 shows a comparison between the experiments and the computational simulation of the time averaged spanwise vorticity for an AoA of $0°$. Good agreement is observed, not only in the magnitude of the vorticity but also in the shape of the vortical structures. Figure 8 shows the instantaneous eddy viscosity field and vorticity field for an AoA of $0°$. It is clear that there is a vortex street in the wake in which the distance between vortical structures is about $\frac{x}{c} = 0.28$. The Strouhal number based on the chord for this simulation is about 3.6. Experimental results show a Strouhal number of approximately 3.8 (Brzozowski et al., 2008).

Figure 9 shows the result of the drag and lift coefficients for these simulations. Since computational results assume infinite aspect ratio and free boundary conditions, experimental data had to be corrected for these effects before comparison to the simulations. This correction takes

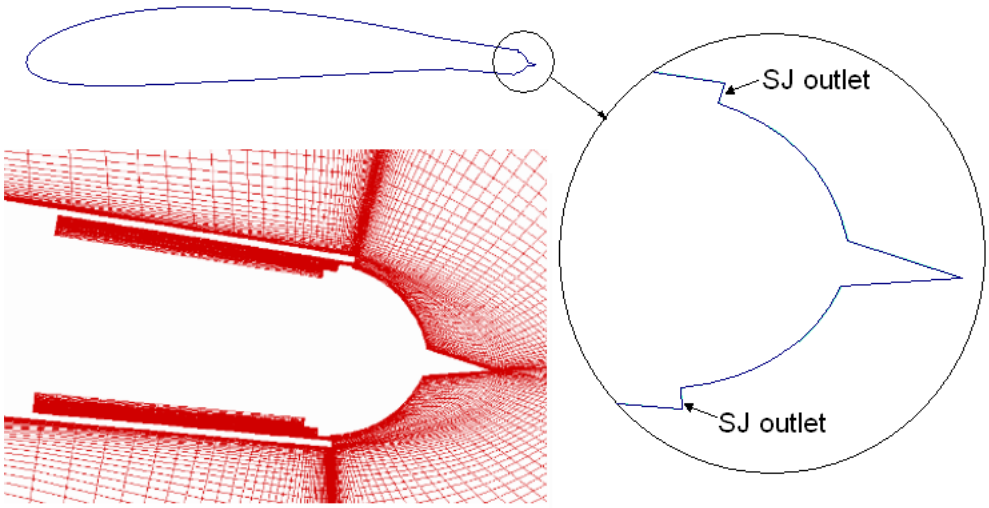

Figure 4: Modified NACA4415

in account the solid and wake blockage, wall effects and infinite aspect ratio. The correction procedure was based on the methodology proposed by Barrow et al. (1999) and Jacobs and Anderson (1931).

5.2 Validation of actuated cases

5.2.1 Detail model

Figure 10 shows the time averaged vorticity field close to the suction side actuator, on the left no actuation on the right actuator active. The actuation Strouhal number based on the chord ($S_{act} = \frac{f_{act}c}{U_\infty}$) used in that simulation was 31.24 (corresponds to 2050 Hz in the experimental set-up at Georgia Tech). The amplitude of the velocity in the Dirichlet boundary condition was $0.014U_\infty$. This amplitude yields a C_μ on the synthetic jet outlet of $O(1e-3)$. The time stepping in this model is limited by the actuation frequency, in this case a time step of $3 \times 10^{-4} \frac{c}{U_\infty}$ was used in order to get about 100 steps per actuation cycle.

Figure 11 shows the effects of the actuator on the moment coefficient (C_m) measured at 0.25c for an AoA of $0°$. The actuator is active after $\frac{tU_\infty}{c} = 7.5$. It is clear that when the suction side (SS) actuator is active there is an increment in the pitch down moment, while there is a reduction of the pitch down moment when the pressure side (PS) actuator is active. Figure 12 shows the effects of the actuator on the lift coefficient (C_l) for the same simulation, when the SS actuator is active there is a reduction of the lift coefficient, while there is an increment of the lift coefficient when the PS actuator is active. For this simulation ($Re = 9 \times 10^5$ and $AoA = 0°$) the increment in the C_m due to the SS actuator is about 0.015 while the reduction in C_l is about 0.07 i.e $\Delta C_l \approx 5\Delta C_m$.

The effectiveness of the actuator is measured by computing the increment or reduction of the the aerodynamic properties of the airfoil, in special the moment and lift coefficient. ΔC_m measures the change in moment coefficient while ΔC_l measures the change in lift coefficient. Figures 13 and 14 show the effectiveness of the actuator (computational and experimental) in the range of $-2°$ to $10°$ with the actuator at full actuation strength [5]. These figures show that the behavior observed at $AoA = 0°$ is similar to the other angles in the range of study. According to

[5]Full actuation is defined by the maximum experimental voltage that could be applied to the piezoelectric elements of the synthetic jet and that produce an RMS velocity at the synthetic jet outlet of about $40\frac{m}{s}$

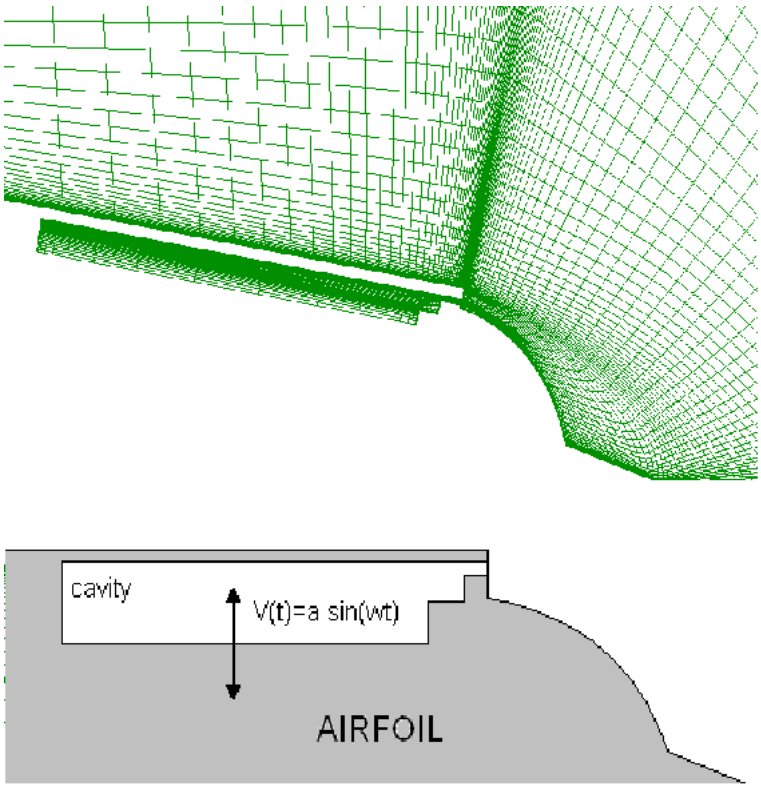

Figure 5: Geometry of the synthetic jet cavity with mesh and detail of the boundary condition

Brzozowski et al. (2008), the trends in those figures is consistent with the increase and decrease in circulation close to the trailing edge of the airfoil due to the trapping of clockwise (SS) and counterclockwise (PS) vorticity. This trapped vorticity leads to a variation in the kutta condition of the airfoil and therefore in its aerodynamic properties. The difference in the slope of the curves (between computational and experimental results) has not been determined yet. Two possible causes of this difference could be: three dimensional effect in the actuators (due to its design) or the behavior of the turbulent model in the region close to the synthetic jet outlet and in the coanda part of the actuator.

Figure 15 shows the variation of the time-averaged pressure coefficient (C_p) along the airfoil. It is noticed the influence of the actuators in the pressure distribution especially at the trailing edge. The increment of C_p, for both the SS and PS actuators, at $\frac{x}{c} = 0.95$ (position of the actuators) is about 0.6 with respect to the unactuated case. Similar results were reported by DeSalvo and Glezer (2007) with the same actuators (using the same momentum coefficient) but in a different airfoil. It is clear that that reduction of the pressure is associated with the trapped vorticity and with a flow acceleration close to the trailing edge. This figure also shows the way the kutta condition of the airfoil is manipulated by the actuators, leading to a change in the aerodynamic properties of the airfoil. Table 1 shows the pressure coefficient (computational and experimental) at different locations along the airfoil. Despite of some differences between the computational and experimental results especially in the SS location, the simulations capture the correct effect of the actuators on the pressure distribution.

Figure 16 shows the evolution of the vorticity and vector field in one actuation cycle. The cycle starts with the outstroke motion of the membrane (Figure 16a). In this stage the fluid is sucked into the actuator's cavity, it is shown that as this is happening a clockwise (CW) vortex is formed over the synthetic jet outlet. The size and strength of the vortex increases as the

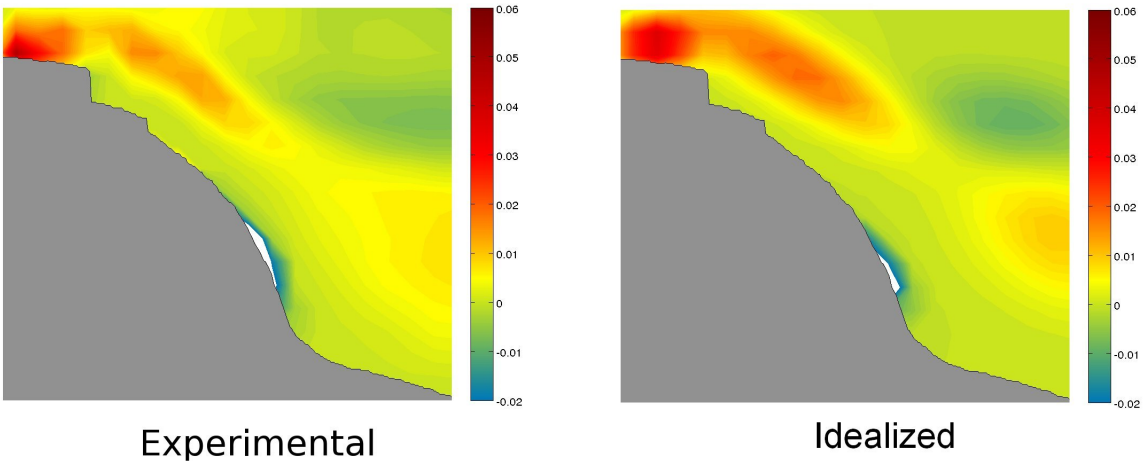

Figure 6: Averaged difference of the u'u' Reynolds stress component

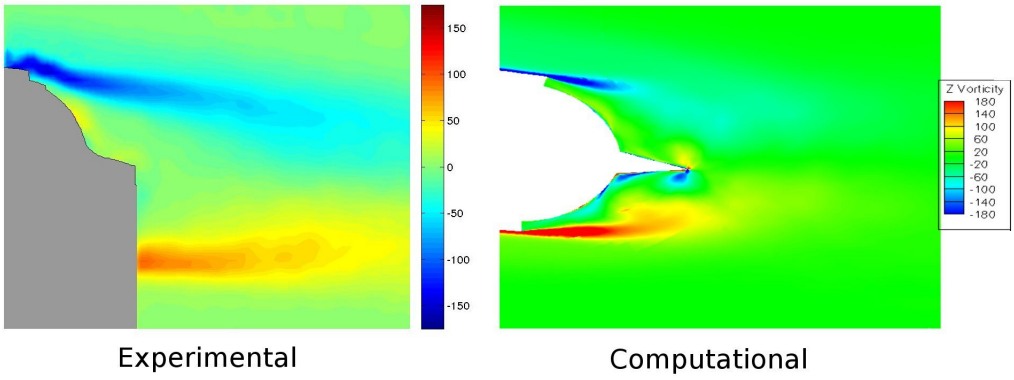

Figure 7: Averaged spanwise vorticity modified NACA4415 at $AoA = 0°$

outstroke finishes as it is shown in Figure 16b. The instroke starts in Figure 16c, at this moment the fluid that is blown out of the cavity interacts with the CW vortex and detached it. As the instroke continues a counterclockwise (CCW) vortex (Figure 16d) is created at the synthetic jet outlet. This CCW vortex is smaller and weaker than the CW vortex of the outstroke phase. Figure 16e shows the end of the instroke phase, were the CCW detaches from the actuator due to the cross flow. Both CW and CCW interact with the wall vorticity and with the shear layer as they are convected downstream. Figure 16f shows the beginning of the outstroke stage, in which the CW vortex starts. Finally, the cycle is completed as it is shown in Figure 16g.

Figure 17 shows the time averaged vorticity field in the near wake for the unactuated (center),

	$\frac{x}{c} = 0.22$ (SS)	$\frac{x}{c} = 0.24$ (PS)	TE
Experimental (no act)	-0.68	-0.18	-0.09
Computational (no act)	-0.80	-0.16	-0.12
Experimental (SS act)	-0.75	-0.16	-0.02
Computational (SS act)	-0.84	-0.14	-0.08
Experimental (PS act)	-0.62	-0.21	-0.07
Computational (PS act)	-0.75	-0.19	-0.05

Table 1: C_p at different locations

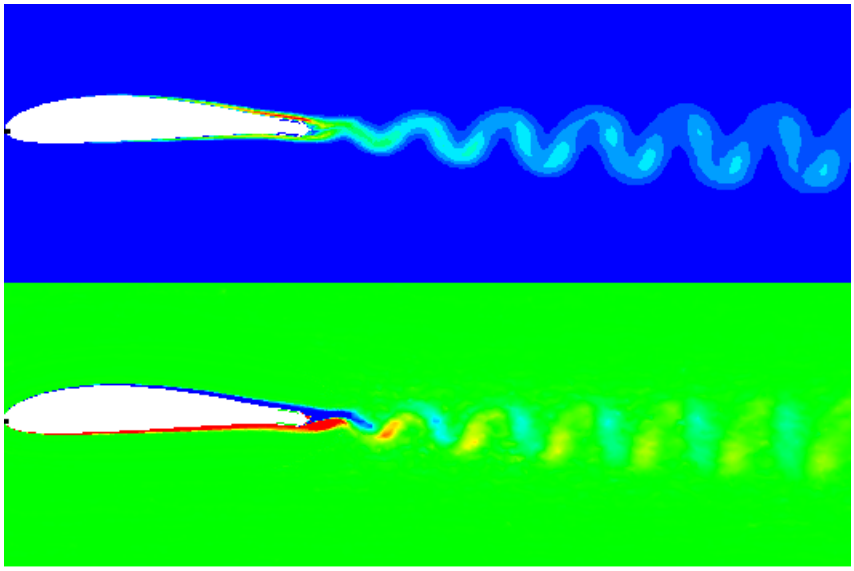

Figure 8: Eddy viscosity (top) and vorticity field (bottom) at $Re = 9 \times 10^5$ and $AoA = 0°$

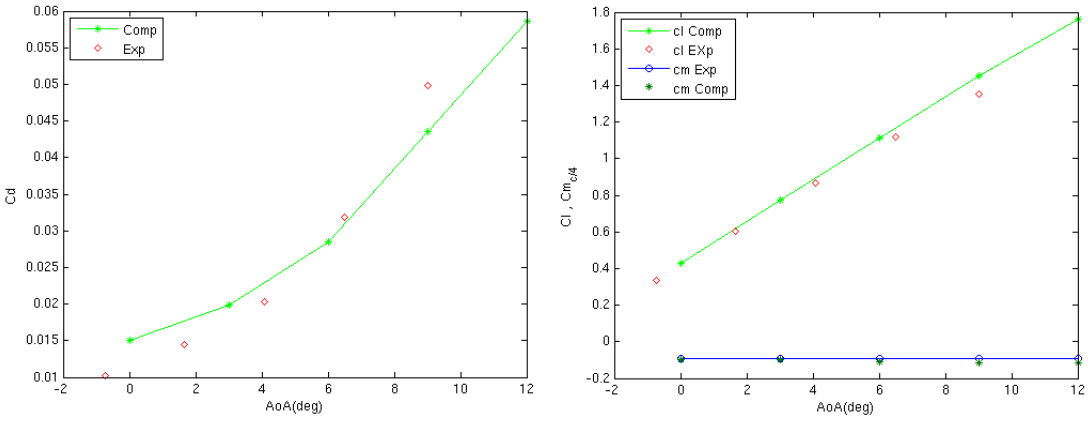

Figure 9: Drag (left) and lift (right) coefficients for the modified NACA4415.

SS actuated (left) and PS actuated (right) cases. In general, it is appreciated that the ”symmetry” of the vorticity field in the near wake, in especial in the coanda part of the actuator, is lost. For the SS actuation, it is clear that the near wake shows a downwash in comparison to the unactuated case. This observation is consistent with the experimental results achieved by Muse et al. (2008). The CW vortical structure is thinner and shorter, while the CCW vortex keeps its topology. For the PS case the near wake shows an upwash, this has been also observed in previous experimental work by Muse et al. (2008). It is also shown that both vortical structures are affected by the PS actuation, they seem thinner and longer than the unactuated case. The effect of the actuators in the wake is more dramatic in the instantaneous vorticity fields. Figure 18 shows the instantaneous vorticity field of the wake for the unactuated (center), SS actuated (left) and PS actuated (right) cases. As discussed in section 5.1, a vortex street is observed for the unactuated case with a shedding frequency of 3.6. For the SS actuation the shedding frequency is affected by the actuation frequency. It is clear that the new shedding frequency is about 6 , the vortices are smaller and the wake is thinner. On the other hand the effect of the PS actuation brings a different effect on the wake, it reduces the vortex shedding substan-

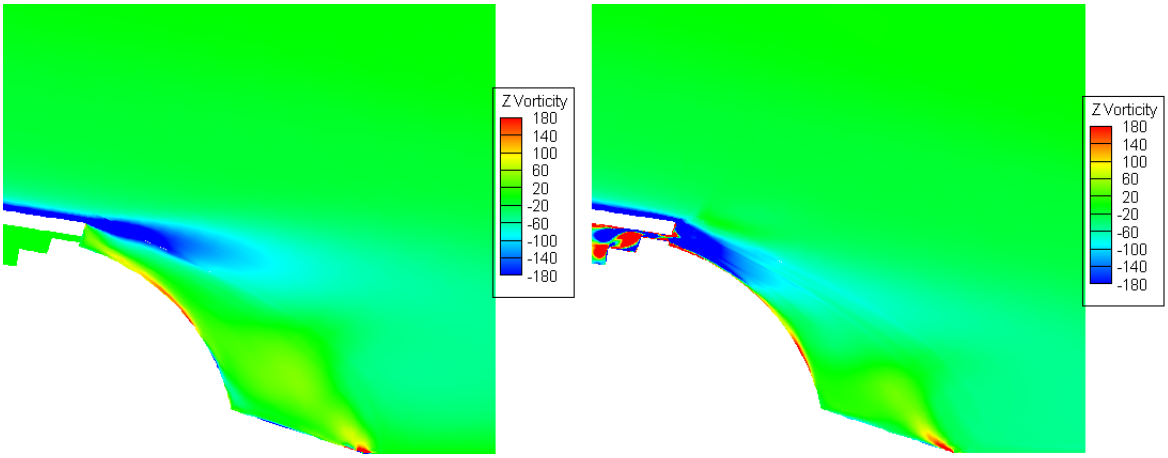

Figure 10: Vorticity field with synthetic jet actuator

tially. A stabilization of the wake is observed after 8 convective time units after the actuation started. This stabilization of the wake has not been corroborated with experiments, nevertheless attenuation of vortex shedding with high frequency actuation has also been observed in other experimental studies. According to Glezer et al. (2005) and Vukasinovic and Glezer (2007) the high frequency actuation increases the dissipation and reduces the turbulent kinetic energy in the wake. This reduction of TKE has been also observed in the experimental setup at Georgia Tech.

5.2.2 RSSJ model

Figure 19 shows a comparison between the experiments and the simulation of the time averaged vorticity field when the actuator is active. One major observed effect is the bending of the vorticity field towards the airfoil surface, this effect is associated with lift enhancement in both experimental and computational results. On the other hand there are two major differences between this two results: First there is a bigger recirculation region in the computational result that is not clearly shown in the experimental PIV data and second there is a stronger vorticity magnitude close to the wall that does not occur in the experimental data. Time stepping in this simulation is limited by stability conditions. In this simulation a time step of $1 \times 10^{-3} \frac{c}{U_\infty}$ was used, so for a given Reynolds number and mesh this model requires a time step about one order of magnitude smaller than the detail one.

6 CONCLUSIONS

A computational study of an airfoil (modified NACA4415) with synthetic jet control was presented. For this purpose, an implementation of the Delayed detached eddy simulation (DDES) turbulent model in a nearly kinetic energy conserving code was required. Two different synthetic jet models were presented: detail and Reynolds stress model. Numerical results demonstrated the effects of the synthetic jets in the flow (specially in the trapped vorticity) and in the aerodynamic properties of the airfoil.

DDES performance in the CDP code is satisfactory as it is shown in the validation of unactuated cases. One of the hardest properties of discretization of the SA equation is the preservation of its positivity, especially in unstructured grids. The preservation of the positivity of the SA equation depends on different factors such as: time discretization, numerical solver and type of grid used. On the other hand, one advantage of using DDES on an standard LES as CDP

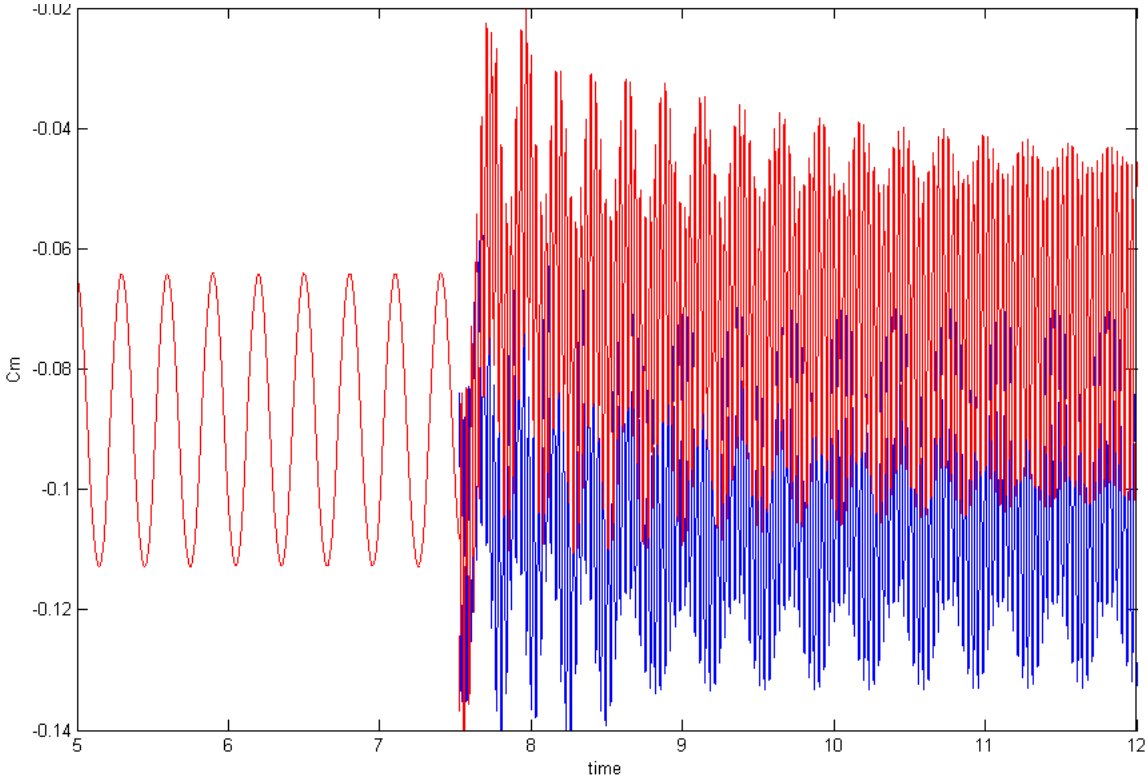

Figure 11: Moment coefficient as a function of time. SS(blue) PS(red)

is the wall treatment, rather than to implement an LES based wall treatment, the RANS model captures the physics of the flow close to the wall. In practice, correct results from DDES can be obtain by switching to Zonal DES (ZDES) or to Extended DDES (EDDES).

Results from the detail model show the effects of the actuator on the aerodynamic properties of the airfoil (in special C_l and C_m). Full actuation of the SS actuator increases the pitch down moment and reduces the lift force, while the PS actuator reduces the pitch down moment and increases the lift force. These observations are explained by the effect of the trapped vorticity concentration on the kutta condition of the airfoil. Trapped vorticity close to the trailing edge of the actuator affects the pressure distribution along the airfoil, this change in the C_p allows the manipulation of the kutta condition and the aerodynamic properties of the airfoil. One relevant observation is the effect of the actuators on the vorticity field, especially in the wake. Instantaneous vorticity field close to the synthetic jet outlet show a pair of counter-rotating vortex that are created in each actuation cycle and advected downstream by the cross flow. This vortices interact with the cross flow vorticity and with the near wall vorticity as well. This periodic injection of vorticity in the flow brings time averaged modifications on the vorticity field in the wake. In the near wake it is observed that the SS actuation downwashes the near wake (close to the trailing edge) while the PS actuation upwashes the near wake in comparison with the unactuated case. Both actuation affects the topology of the vortical structures observed in the time averaged vorticity field. The instantaneous vorticity field in the far wake showed two different effects for the PS and the SS actuation. While the PS actuation attenuates the vortex shedding and stabilizes the wake, the SS actuation increases the vortex shedding frequency. These observations have not been corroborated experimentally but some previous research shows similar results in the reduction of the vortex shedding frequency of bluff bodies.

Two possible causes of the difference between the numerical and experimental results in the

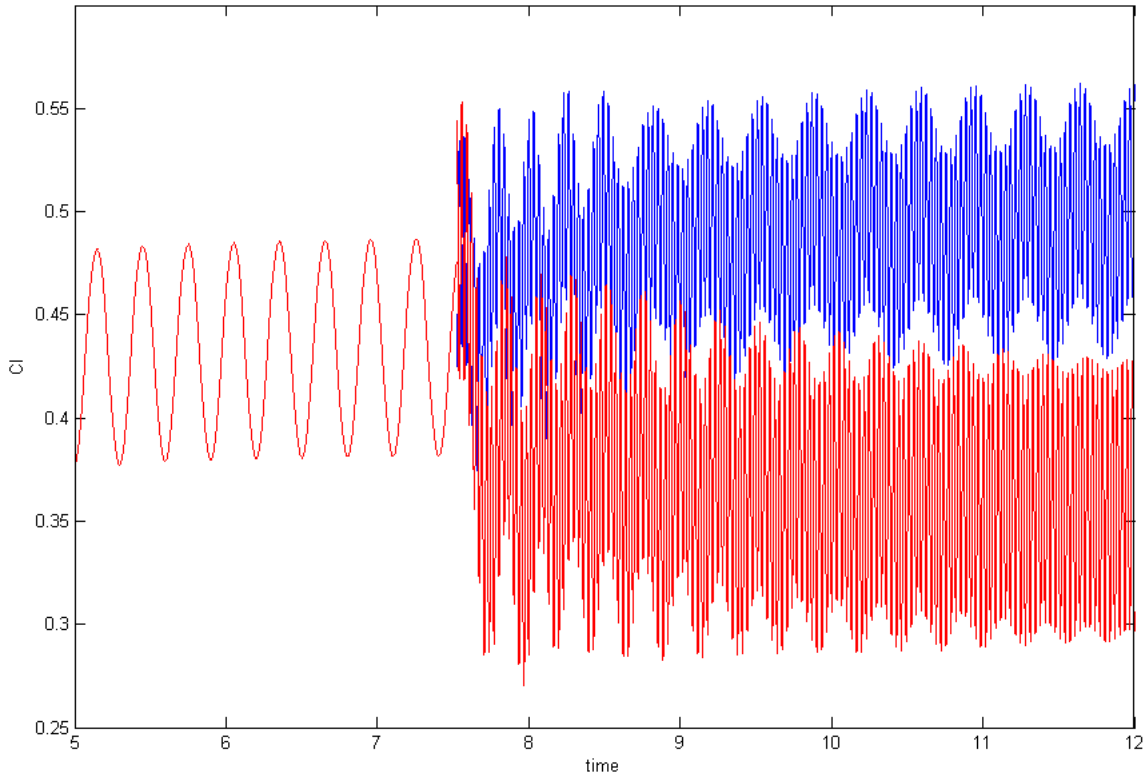

Figure 12: Lift coefficient as a function of time. SS(blue) PS(red)

effectiveness of the actuator at higher AoA could be: three dimensional effect in the actuators (due to its design) or the behavior of the turbulent model in the region close to the synthetic jet outlet and in the coanda part of the actuator. Current research is focused towards the 3D effect of the actuator ends and also in the implementation of the Extended DDES model to improve the turbulent model behavior especially in the coanda part of the actuator and in the synthetic jet outlet.

While the RSSJ model reduces the complexity of the simulation (geometry and boundary conditions) in comparison with the detail model, it just captures the average behavior of the synthetic jet. The detail model fully captures the dynamics of the synthetic jet actuator but it increases the complexity of the simulation due to the cavity geometry and extra boundary conditions. The most important advantage of using the RSSJ model instead of the detail model is that for a given mesh it reduces the time step about one order of magnitude. This observation is consistent with the fact that the time stepping in the detail model is limited by the synthetic jet frequency while the time stepping in the RSSJ model is limited by stability/accuracy of the numerics. RSSJ result seems promising and future work includes the characterization the effects of the jet strength and external parameters such as free stream velocity and angle of attack.

7 ACKNOWLEDGEMENT

- As part of the AVOCET project, this work has been supported by the Air Force Office of Scientific Research and Multidisciplinary University Research Initiative (AFOSR-MURI).
- Dr Glezer's research group at Georgia Tech for providing the experimental data.
- Center for Integrated Turbulence Simulation (CITS) for providing the CDP code v2.3.

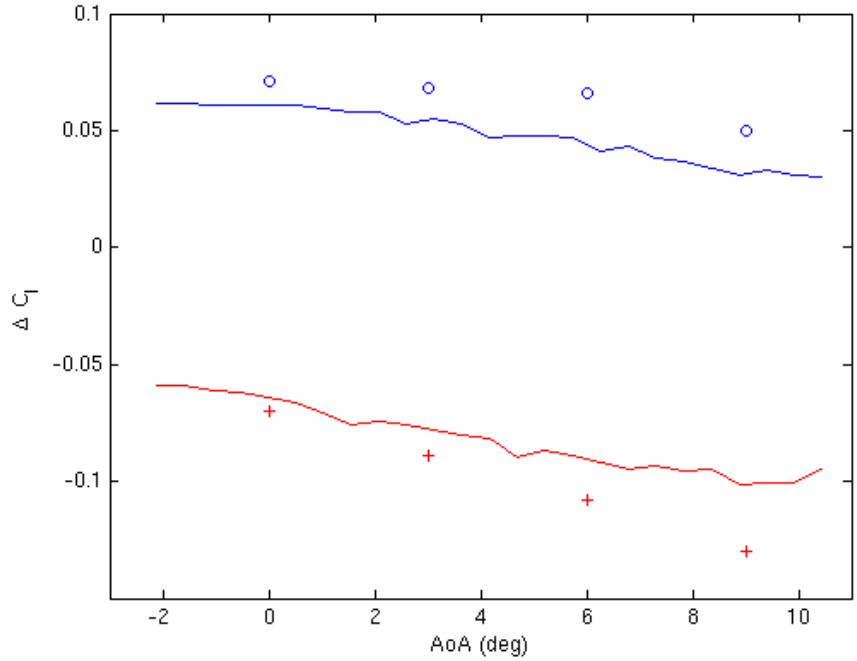

Figure 13: Lift coefficient as a function of AoA. (SS exp – PS exp– SS comp ∘ PS comp +)

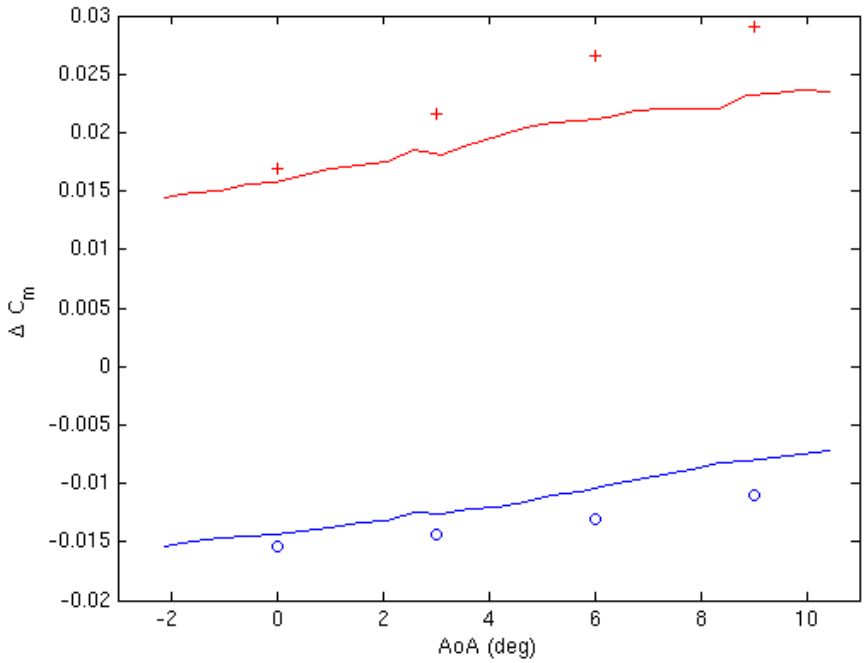

Figure 14: Moment coefficient as a function of AoA. (SS exp – PS exp– SS comp ∘ PS comp +)

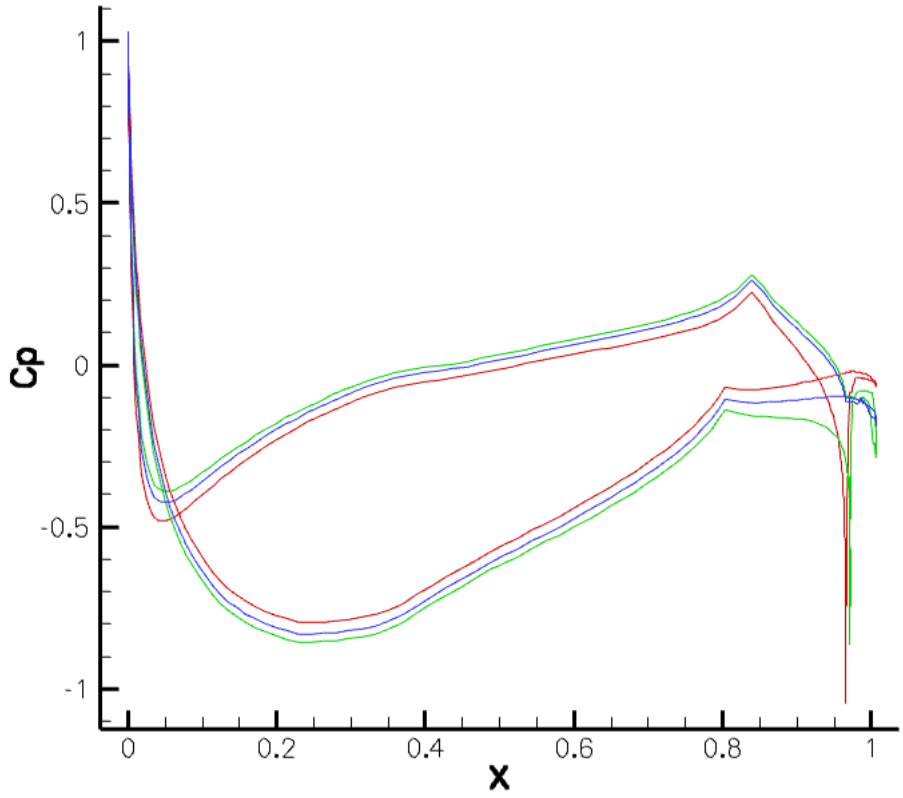

Figure 15: Pressure coefficient at $AoA = 0°$. (SS – PS – no act –)

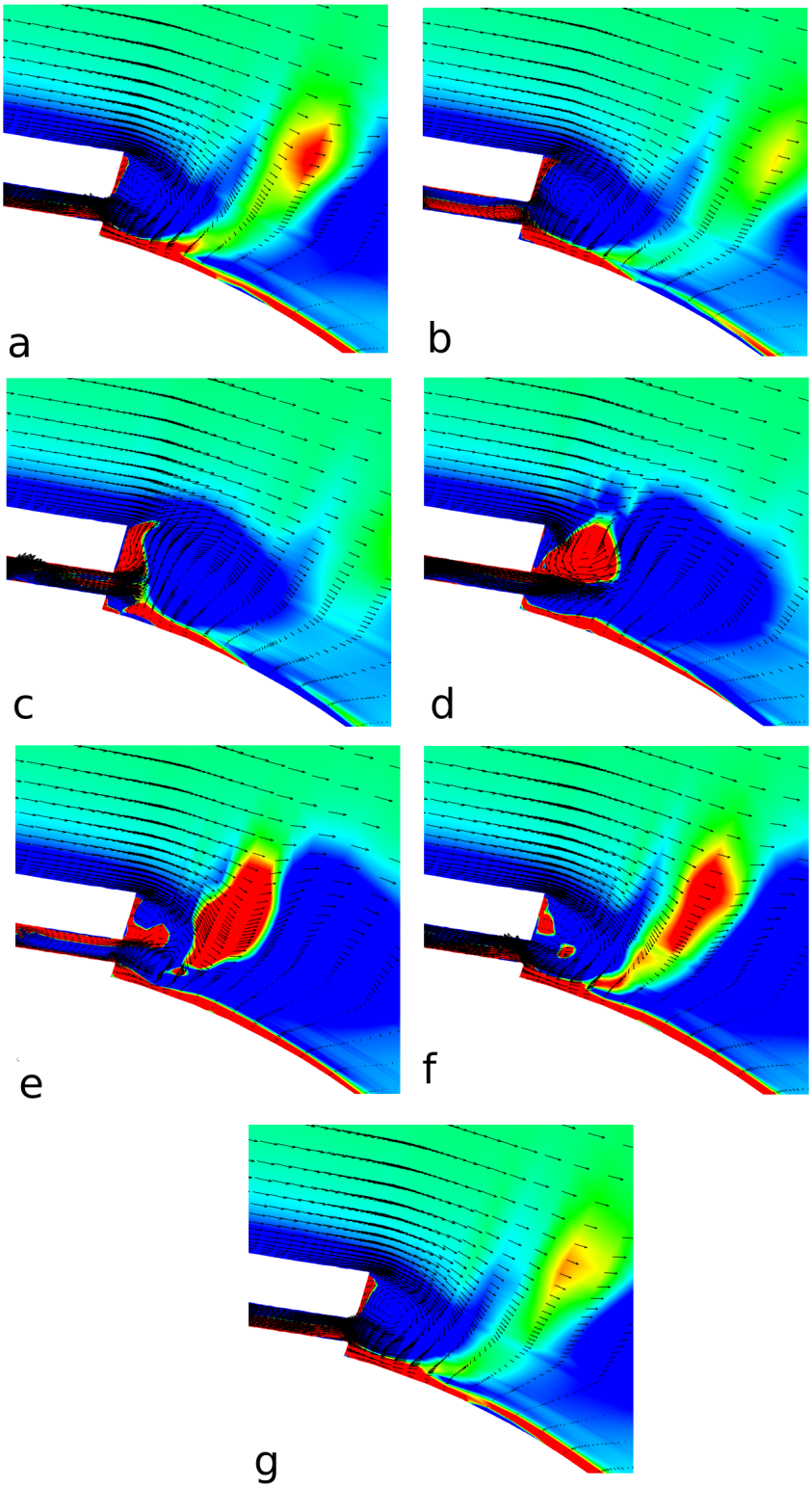

Figure 16: Evolution of the vorticity and vector field close to the synthetic jet outlet

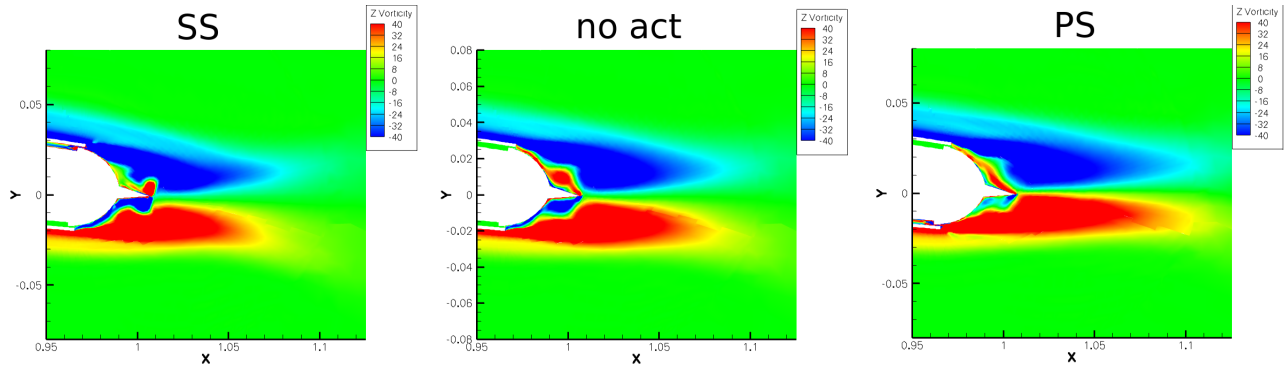

Figure 17: Time averaged vorticity field in the near wake ($AoA = 0\circ$). SS actuation (left), no actuation (center) and PS actuation (right)

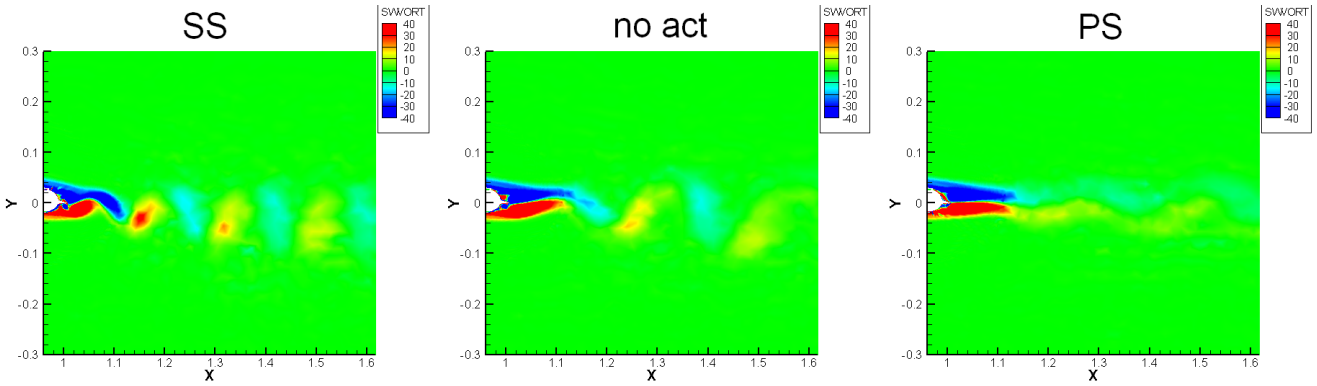

Figure 18: Instantaneous vorticity field in the wake ($AoA = 0\circ$). SS actuation (left), no actuation (center) and PS actuation (right)

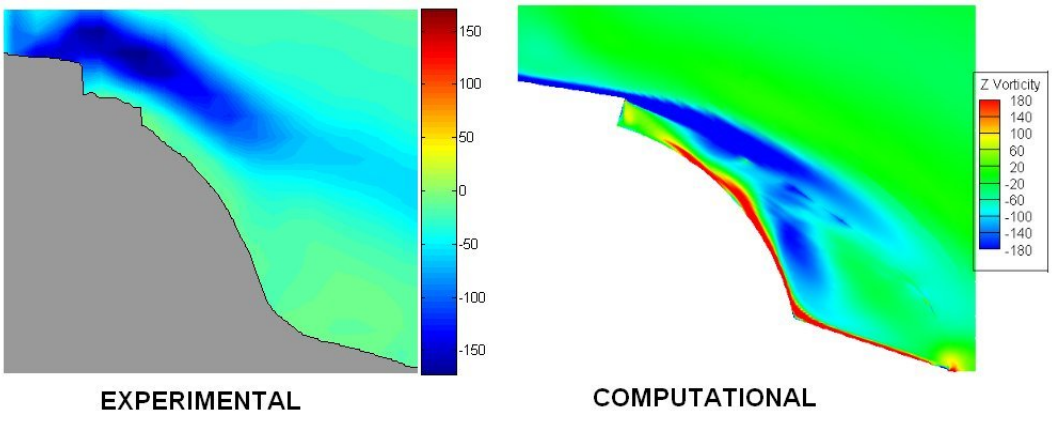

Figure 19: Averaged vorticity field with the actuator on (RSSJ model).

REFERENCES

M. Amitay, D. Smith, V Kibens, D. Parekh, and A. Glezer. Aerodynamic flow control over an unconventional airfoil using synthetic jets actuators. *AIAA Journal*, 39:361–370, 2001.

J. Barrow, W. Rae, and A. Pope. *Low-Speed Wind tunnel testing*. John Wiley and Sons, 1999.

M Breuer, N. Jovicic, and K. Mazaev. Comparison of des, rans and les for the separated flow around a flat plate at high incidence. *International Journal for Numerical Methods in Fluids*, 41:357–388, 2003.

D. Brzozowski and A.Glezer. Transient separation control using pulse-combustion actuation. In *3rd AIAA Flow Control Conference*, 2006. AIAA-2006-3024.

D. Brzozowski, J. Culp, A. Kutay, J. Muse, and A. Glezer. Closed-loop aerodynamic flow control of a free airfoil. In *AIAA 4th Flow Control Conference*, 2008. AIAA-2008-4323.

S. Deck. Zonal-detached-eddy simulation of the flow around a high-lift configuration. *AIAA Journal*, 43:2372–2384, 2005.

S. Deck. Delayed detached-eddy simulation of self sustained unsteadiness and side-loads in an over expanded nozzle. Submitted to Shock Waves, 2008.

S. Deck, P. Duveau, P. d'Espiney, and P. Guillen. Development and application of spalart-allmaras one equation turbulence model to three-dimensional supersonic complex configurations. *Aerospace Science and Technology*, 6:171–183, 2002.

M. DeSalvo and A. Glezer. Control of airfoil aerodynamic performance using distributed trapped vorticity. In *AIAA 45th Aerospace Sciences Meeting and Exhibit*, 2007. AIAA-2007-708.

M.E. DeSalvo and A. Glezer. Aerodynamic performance modification at low angles of attack by trailing edge vortices. In *2nd AIAA Flow Control Conference*, 2004. AIAA-2004-2118.

Q. Gallas, R. Holman, T. Nishida, B. Carroll, M. Sheplak, and L. Cattafesta. Lumped element modeling of piezoelectric-driven synthetic jet actuators. *AIAA Journal*, 41:240–247, 2003.

A. Glezer, M. Amitay, and A. Honohan. Aspects of low and high frequency actuation for aerodynamic flow control. *AIAA Journal*, 43:1501–1511, 2005.

A. Gross and H. Fasel. Cfd for investigating active flow control. In *AIAA 4th Flow Control Conference*, 2008. AIAA-2008-4310.

R. Holman, Y. Utturkar, R. Mittal, B. Smith, and L. Cattafesta. Formation criterion for synthetic jets. *AIAA Journal*, 43:2110–2116, 2005.

L. Huang, P. G. Huang, R. P. LeBeau, and T. Hauser. Numerical study of blowing and suction control mechanism on naca0012 airfoil. *Journal of Aircraft*, 41:1005–1013, 2004.

G. Iaccarino and F. Ham. Automatic mesh generation for les in complex geometries. Technical report, Center for Turbulent Research, Stanford University, 2005.

U. Ingard. On the theory and design of acoustic resonators. *The Journal of the Acoustical Society of America*, 25:1037–1061, 1953.

E. Jacobs and R. Anderson. Large-scale aerodynamic characteristics of airfoils as tested in the variable density wind tunnel. Technical Report 352, NACA, 1931.

G. Karypis and V. Kumar. Parmetis: Parallel graph partitioning and sparse matrix ordering library. Technical Report 97-060, Department of Computer Science, Univ. of Minnesota, 1997.

E. Lorin, A. Hajlai, and A Soulaimani. An accurate positivity preserving scheme for the spalart-allmaras turbulence model. application to aerodynamics. In *36th AIAA Fluid Dynamics Conference and Exhibit*, 2006. AIAA-2006-3743.

K. Mahesh, G. Constantinescu, and P. Moin. A numerical method for large-eddy simulation in

complex geometries. *Journal of Computational Physics*, 197:215–240, 2004.

R. Mittal and L. Cattafesta. Actuator flow physics and its implication for cfd modeling of znmf jet based separation control. In *AIAA 4th Flow Control Conference*, 2008.

P. Moin and S. Apte. Large-eddy simulation of realistic gas turbine combustors. In *42nd AIAA Aerospace Sciences Meeting and Exhibit*, 2004. AIAA-2004-330.

Y. Morishini, T. Lund, O. Vasilyev, and P. Moin. Fully conservative higher order finite difference schemes for incompressible flow. *Journal of Computational Physics*, 143:90–124, 1998.

J. Muse, A. Kutay, D. Brzozowski, D. Calise, and A. Glezer. Dynamic flight maneuvering using trapped vorticity flow control. In *AIAA 46th Aerospace Sciences Meeting and Exhibit*, 2008. AIAA-2008-0522.

D. Parekh, S. Williams, M. Amitay, A. Glezer, A. Washburn, I. Gregory, and R. Scott. Active flow control on the stingray uav: Aerodynamic forces and moments. In *33rd Fluid Dynamics Conference and Exhibit*, 2003. AIAA-2003-4002.

C. Rumsey. Sucesseses and challenges for flow control simulations. In *AIAA 4th Flow Control Conference*, 2008. AIAA-2008-4311.

M. Shur, P Spalart, M. Strelets, and A. Travin. Detached-eddy simulation of an airfoil at high angle of attack. In *4th International Symposium on Engineering Turbulence Modelling and Measurements*, pages 669–678, 1999.

B. Smith and A. Glezer. The formation and evolution of synthetic jets. *Physics of Fluids*, 10: 2281–2297, 1998.

P. Spalart and R. Allmaras. A one-equation turbulence model for aerodynamics flows. *La Recherche Aerospatiale*, 1:5–21, 1994.

P. Spalart, W. Jou, M Strelets, and S. Allmaras. Comments on the feasibility of les for wings, and on a hybrid rans/les approach. In *Advances in DNS/LES*, pages 137–147, 1998. First AFSOR International Conference on DNS/LES.

P. R. Spalart. Young-person's guide to des grids. Technical Report CR-2001-211032, NASA, 2001.

P.R. Spalart, S. Deck, M. Shur, K Squires, M. Strelets, and A. Travin. A new version of des resistant to ambiguous grid densities. *Theoretical and Computational Fluid Dynamics*, 20: 181–195, 2006.

K. Squires, J. Forsythe, S. Morton, D. Blake, M. Serrano, K. Wurtzler, W. Strang, R. Tomaro, and P. Spalart. Analysis of full aircraft with massive separation using detached-eddy simulation. In *Department of Defense High Performance Computing User Group Conference*, 2002.

D. Von Terzi, J. Frohlich, and I Mary. Zonal coupling of les with downstream rans calculations. Submitted to Theoretical and Computational Fluid Dynamics, 2006.

E. Touber and R. Moser. Modeling approach for a 2d synthetic jet. In *Bulletin of the American Phisical Society*, 2006.

A. Travin, M. Shur, M. Strelets, and P. Spalart. Detached-eddy simulations past a circular cylinder. *Flow, Turbulence and Combustion*, 63:293–313, 1999.

J. Vadillo and R. Agarwal. Numerical study of aerodynamic performance of airfoils at low angles of attack by active flow control of trailing edge vortices. In *44th AIAA Aerospace Sciences Meeting and Exhibit*, 2006. AIAA-2006-1058.

B. Vukasinovic and A. Glezer. Control of a separating flow over a turret. *AIAA Paper 2007-4506*, 2007.

P.J. Zwart. *The integrated space-time finite volume method*. PhD thesis, University of Waterloo, 1999.